MODELING AND OPTIMIZATION OF PROCESS PARAMETERS FOR FRICTION STIR WELDING OF DISSIMILAR AEROSPACE ALLOYS AA2014 AND AA7075

Raj Kumar[1] – Vikas Upadhyay[1] – Chaitanya Sharma[2*]

[1]Mechanical Engineering Department, National Institute of Technology Patna, Patna-800005, India
[2]Mechanical Engineering Department, BIT Sindri, Dhanbad, Jharkhand-828123, India

ARTICLE INFO	Abstract:
	Aluminum alloys possess a high strength-to-weight ratio and good corrosion resistance making them suitable for various structural parts and components used in the aerospace industry. However, the principal barrier restricting their use is their weldability. This experimental study addresses the issues in joining of dissimilar aerospace aluminum alloys. In this work, friction stir welding (FSW) of dissimilar high strength alloys AA2014 and AA7075 has been carried out and the effect of welding parameters has been studied to obtain defect-free high strength welds. Detailed statistical analysis was performed and suitable regression models were developed for prediction and optimization. Multi-objective optimization has been carried out by employing the desirability function to determine the optimal condition for defect-free welds with adequate mechanical properties. Microstructure and fracture surface of the optimum weld was also studied and compared with the lowest and highest heat input welded joints.

1   Introduction

Among various aluminum alloy series, 2XXX (Cu alloy) and 7XXX (Zn alloy) represent a gamut of high strength heat-treatable alloys that are suitable for use in the aerospace industry [1]. AA7075 and AA2014 are widely used high-strength alloys in the aerospace industry i.e. AA7075 is used to make upper wing parts, floors, body stiffeners of airplanes whereas AA2014 is widely used in aircraft structure [2], [3]. The high strength of these alloys is mainly attributed to precipitate hardening. The main strengthening precipitates that derive the strength of AA2014 are Al_2Cu and Al_2CuMg while for AA7075 the strengthening precipitates are $MgZn_2$ and Al_2CuMg respectively [3]-[6].

FSW is widely utilized in various industrial sectors such as aerospace, automotive, shipbuilding, railway, and marine because of its ability to form joints in solid-state as the maximum temperature during welding is in the range of 0.60 to 0.95 times of base metal's melting point [7]-[14]. Also, in comparison to defects developed in fusion welds such as porosity, shrinkage, or embrittlement it results in reduced defects and less distortion in the welded joints [15]-[19]. Joining dissimilar alloys is difficult due to the different physical, chemical and mechanical properties of two alloys to be joined together [20]-[23]. Increased requirement of dissimilar joints and several advantages of the FSW process has encouraged aerospace, rail, automotive, and shipbuilding industries to adopt this process for joining dissimilar aluminum alloys [1]. A brief review of the literature, in line with the present work, has been presented below.

The effect of WS and location of the base metal during the welding of AA2024 and AA7075 was reported by Khodir and Shibayanagi [24]. The highest strength was obtained for the joint formed at WS of 102 mm/min with AA2024 on the advancing side. Da Silva et al. [25] studied the effect of rotational speed (RS) on material flow and mechanical behavior of AA2024-T3 and AA7075-T6 in dissimilar FSW. The RS of 400 rpm, 1000 rpm, and 2000 rpm at a fixed welding speed (WS) of 254 mm/min were used to produce the welds.

---

* Corresponding author
E-mail address: cs.me@bitsindri.ac.in

The maximum value of ultimate tensile strength (UTS) was 443 MPa at RS of 1000 rpm. Material mixing was found dependent on RS, as at low RS onion rings were not formed but with an increase in RS, the onion rings start to appear in the weld nugget zone (WNZ). Hasan et al. [26] examined the effect of flute radius of tool pin and placement of base metal alloy on microstructure and mechanical properties of AA2024 and AA7075 welds. The tool pin with a flute radius of infinity, 0, 2, 3, and 6 mm was used to produce dissimilar joints.

The highest strength was reported when the flute radius was equal to the pin radius of the tool (3 mm). Khan et al. [2] studied the effect of various RS on microstructure and its influence on microhardness in FSW of AA2219-O and AA7475-T761 alloys. Low strength alloy (AA2219-O) was placed on the advancing side whereas high strength alloy (AA7475-T761) was placed on the retreating side. They observed that microhardness value increased with increasing RS on the retreating side and decreased on the advancing side. In WNZ, dissolution and re-precipitation of strengthening precipitate occurred at higher RS. Tool pin profile effect on mechanical properties and formability of welds of AA2014 and AA6061 was examined by Nadikudi et al. [27]. The tool pin profiles used at fixed welding parameters in the experiment trials are straight-cylindrical, taper-cylindrical, stepped-cylindrical, straight-square, and straight-hexagon. It was reported that the best mechanical properties and formability of the welded joint were obtained with a straight square tool pin profile as it produces a pulsating effect that results in fine grain formation at the WNZ. Alvarez et al. [28] investigated the material flow and mixing pattern in FSW of AA7075-T6 and AA2024-T3 by varying the RS from 400 to 2000 rpm at a fixed WS of 254 mm/min. Optimum mechanical properties were observed at low RS whereas at high RS, despite intense mixing and formation of onion ring-like pattern, surface integrity was reduced. Jonckheere et al. [29] examined the effect of RS, base metal location, and tool shift on power, torque, and temperature in FSW of AA6061 and AA2014. Power, torque, and temperature of dissimilar joints were found in between similar joints of AA2014 and AA6061. Tool shift of 2 mm towards AA2014, produced better results in comparison to tool shift towards AA6061. Sharma et al. [30] studied the tensile properties of AA2024 and AA7039 dissimilar joints. Localized stress concentration was reported as the main cause of low strength and ductility of welded joints. Barbini et al. [31] examined the experimental effects of varying WS at fixed RS and alloys positions in dissimilar FSW of AA2024 and AA7050. High strength was obtained when low strength alloy was placed at the advancing side because of the better material flow and at lower WS. Saravanan et al. [32] studied the effect of the welding parameter and diameter of shoulder to diameter of pin (D/d) ratio in FSW of AA2014-T6 and AA7075-T6. It was concluded that maximum strength was obtained by placing the AA2014 on the advancing side at RS of 1200 rpm, WS of 20 mm/min, and D/d ratio of 3. Singh and Dhuria [33] studied the effect of post-weld cryogenic treatment on weld strength of dissimilar alloy combination of AA2014-T651 and AA7075-T651 and reported a marginal improvement in mechanical properties. Pandian and Kannan [34] developed numerical models for temperature distribution and grain size of dissimilar welds and also verified them experimentally.

Response surface methodology was used in numerous studies for the modelling and optimization of FSW process parameters [35]-[40]. Heidarzadeh et al. (2012) [35] selected three input parameters for central composite rotatable design of response surface methodology (RSM) which are rotational speed, welding speed and axial force with five levels. The output parameters were hardness and yield strength. It was concluded that the maximum tensile strength was obtained at RS of 920 rpm, WS of 78 mm/min, axial force of 7.2 kN while maximum elongation was obtained at RS of 1300 rpm, WS of 60 mm/min and axial force 8 kN force.

Ample studies have been carried out on 2xxx and 7xxx series alloys, but particularly for dissimilar welds of AA2014 and AA7075few studies were carried out. Moreover, a systematic study on the effect of welding speed and rotary speed in dissimilar welds of AA2014 and AA7075 was not carried out. The present work has two-fold objectives, first is to develop regression models and determine the optimal welding parameters and the second is to study the effect of RS and WS on mechanical properties of FSW joints of AA2014 and AA7075 aerospace alloys.

2 Experimental investigation

Two dissimilar high strength heat-treatable alloys, AA2014 and AA7075 in T6 temper were friction stir welded in butt position. Plates to be welded were of 6 mm thickness, 140 mm length, and 50 mm width. The chemical composition of base metals along with their mechanical properties are enlisted in Table 1.

Table 1. Chemical composition and mechanical properties of AA2014 and AA7075.

Alloy	Chemical composition (wt%)								Mechanical Properties		
	Si	Fe	Cu	Mn	Mg	Cr	Zn	Al	Ultimate tensile strength (MPa)	Elongation (%)	Microhardness (HV)
AA2014	0.52	0.37	4.71	0.86	0.25	-	-	Bal.	469.31	7.82	156.43
AA7075	-	0.32	1.56	-	2.26	0.22	6.25	Bal.	553.63	9.38	173.29

A circular bar of H13 grade die-steel was used to fabricate the tool as per details given in Table 2. The shoulder surface has a concavity of 6°, and the pin has threads of 1 mm pitch. Experiments were performed on a computer-controlled vertical milling machine. The abutting edges of plates were lightly rubbed with emery paper to remove oxides and foreign particles and then cleaned with acetone to remove carbon dust from the edges. The weaker metal of the combination i.e. AA 2014 was kept on the advancing side to develop the welds.

Table 2. Details of tool geometry and welding parameters.

Tool dimensions			Welding parameters						
Shoulder diameter (mm)	Pin diameter (mm)	Pin length (mm)	Welding Speed (mm/rev)			Rotational Speed (rpm)			Tool tilt (º)	Dwell time (s)
20	6	5.7	60	120	180	600	1000	1400	0	15

Three tensile tests for each parametric combination have been carried out on a computerized universal testing machine (load capacity 50 kN) with a strain rate of 1 mm/min. The tensile samples were prepared as per the ASTM E8/E8M-21 standard. Samples preparation for microstructure has been done by polishing the welded samples and etching with the Keller's reagent (3 ml of HNO_3, 6 ml of HCl, 6 ml of HF, and 150 ml of water) for 20 s. The microscopic study of the welded samples has been performed by an optical microscope. The fractured surface of tensile samples was studied with the help of a Scanning electron microscope (SEM).

Experiments were conducted as per the Central composite design (CCD) of Response surface methodology (RSM) consisting of three center points. The design of experiments in coded and actual factors is presented in Table 3. Data of these experiments were then utilized to generate the empirical models for prediction as wells as to analyze the effect of process parameters on responses.

Table 3. Design of Experiments in terms of coded and actual factors.

Experiment Number	Coded Factors		Actual Factors	
	A: WS	B: RS	A: WS	B: RS
1	0	0	120	1000
2	1	−1	180	600
3	0	0	120	1000
4	0	0	120	1000
5	−1	1	60	1400
6	0	−1	120	600
7	0	1	120	1400
8	1	0	180	1000
9	−1	0	60	1000
10	1	1	180	1400
11	−1	−1	60	600

3 Results and discussion

The developed welds were visually inspected for the presence of any defect. All the welds except for the weld formed at lowest heat input (LHI) parameters i.e. RS of 600 rpm and WS of 180 mm/min appeared to be defect-free in visual inspection. The macrostructure of the weld cross-section corresponding to the lowest and highest heat input parameters (HHI) has been presented in Figure 1. The shape of the stir zone was inverted trapezoidal for the HHI weld sample whereas the LHI weld sample displayed roughly rectangular i.e. straight stir zone with vertical transition boundary. Improper material mixing and flow due to inadequate heat input at the LHI set of welding parameters resulted in macroscopic defect formation on the advancing side. However, during the microscopic study, some very fine defects were also observed for welding speed of 120 mm/min and 180 mm/min at all investigated range of RS. One such microscopic defect obtained at WS of 120 mm/min and RS of 1000 rpm is shown in Figure 2 a. Figure 2 b summarizes the effect of various parameters on defect formation and depicts that RS did not change the type of defect except for the highest welding speed.

The WS had a significant influence on the formation of defects. An increase in WS resulted in the creation of micro and macro size defect at mid and high WS respectively. These scattered tiny pores of a few microns were believed to form owing to poor consolidation due to faster traverse of the tool without tilt. Use of excessively high WS at fix RS formed void defect on advancing side below the top surface. The size of the void defect increased with an increase in WS because of reduced material flow to weld bottom since flowability was reduced owing to low heat input. Further, faster tool spent less time to consolidate the material [41].
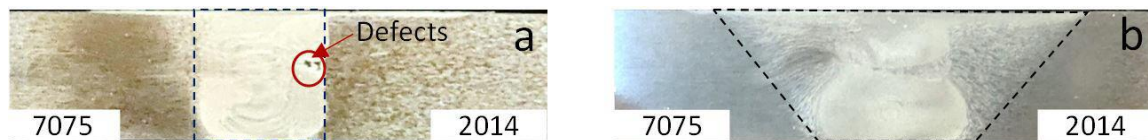

Figure 1. Macrostructure of transverse cross-section of welded joints at (a) lowest heat input parameter [RS= 600 rpm; WS = 180 mm/min] and, (b) highest heat input parameter [RS = 1400 rpm; WS = 60 mm/min].
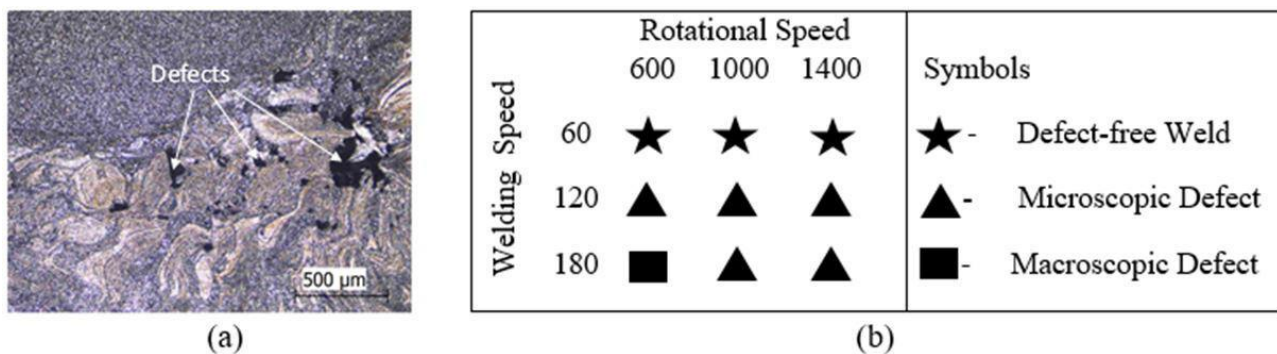

Figure 2. (a) Microscopic defect obtained on the advancing side at WS = 120 mm/min and RS = 1000 rpm and, (b) effect of welding parameters on defect formation.

During FSW, a combination of severe plastic deformation and heat generation produces massive alteration of base metal microstructure, resulting in different zones viz heat-affected zone (HAZ), thermo-mechanical affected zone (TMAZ), and weld nugget zone (WNZ). These zones can be easily distinguished in welds by their orientation and grain size. The microstructure of different zones formed on advancing as well as on the retreating side at the mid-value of WS and RS i.e. 120 mm/min and 1000 rpm respectively are shown in Figure 3. Severe plastic deformation and frictional heating generate the highest heat in WNZ resulting in a very fine microstructure because of the dynamic recrystallization of grains.

The WNZ of welded joints contains alloying elements of both the base metals because of their mixing in solid-state. Rotating tool dragged the material from leading side to trailing side whereas simultaneous traversing of tool caused the material consolidation i.e. flow in batches at the trailing end leading to the formation of onion rings in WNZs of welds. Therefore, onion rings presented an alternate arrangement of dark and bright rings/layers on the transverse surface of welds. These alternate rings were mainly comprised of one

metal and the gap between two consecutive onion rings decreased in the outward radial direction (Figure 4). The brighter color band in an onion ring or vortex-like shape is AA7075 and the darker color band is AA2014 and can be attributed to insufficient mixing and incomplete diffusion.
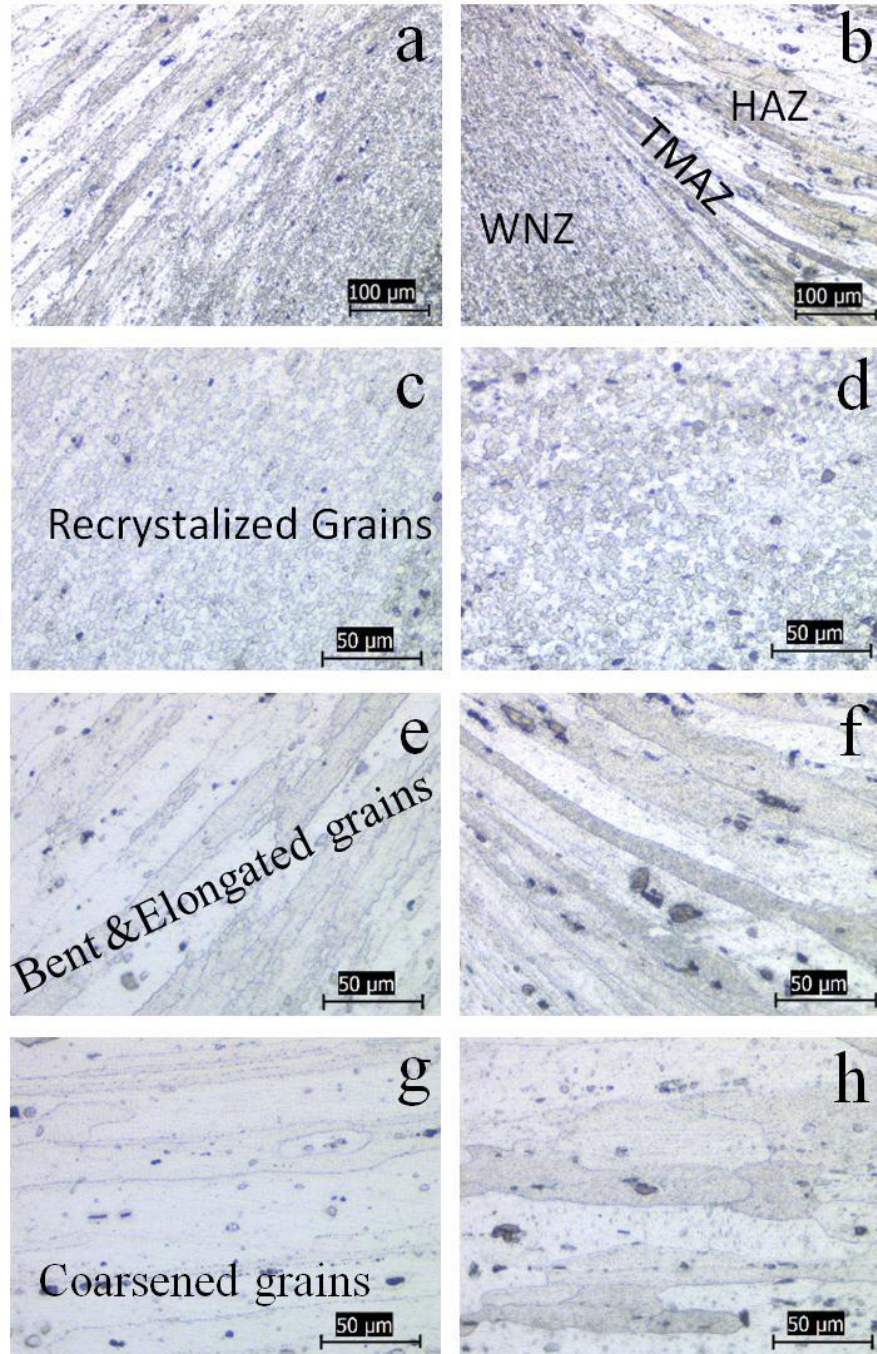

Figure 3. Microstructure of dissimilar joint produced at WS = 120 mm/min and RS = 1000 rpm: (a) Transition from WNZ to Base Metal in AA7075, (b) Transition from WNZ to Base Metal in AA2024 (c) AA7075 WNZ, (d) AA2024 WNZ, (e) AA7075 TMAZ, (f) AA2024 TMAZ, (g) AA7075 HAZ and, (h) AA2024 HAZ.

Grain size on the retreating side (AA7075) was finer than on the advancing side (AA2014) of WNZ and varied from ~ 2 to 3 μm. Varying plastics strains are responsible for this asymmetry in WNZ grain size. The direction of RS and WS was the same on the advancing side and opposite on the retreating side due to the arrangement of plates and direction of rotation and traverse. Therefore, material placed on the advancing side

experienced higher temperature as well as plastic deformation than the retreating side leading to asymmetry in WNZ grain size i.e. slightly larger grain size on the advancing side than the retreating side [42]–[44]. The transition of microstructure from WNZ to TMAZ was sharp on the advancing side due to an abrupt decrease in grain size and gradual on the retreating side. In advancing side, continuous dynamic recrystallization of grain (CDRX) was observed as shown in circled in Figure 5(a), the initial larger grains were followed by the smaller grains while in retreating side discontinuous dynamic recrystallization (DDRX) occured as the grain swell at the grain boundary as evident from in Figure 5(b). Heidarzadeh et al. (2020) [9] also have the same observations. Also the microstructure evolution in friction stir welded 7XXX series aluminium alloys is reported to follow DDRX [45]-[47].

In TMAZ, mechanical and thermal deformation occurred, but the generated temperature was lower than the WNZ, due to which recrystallization did not occur hence deformed grains were observed in this zone having an orientation toward the WNZ of dissimilar welds. However, on the retreating side partial recrystallization is also evident (Figure 3 a & e). In HAZ, only thermal heating of grain occurred due to which original grain structure of the base metals coarsened in this zone on both sides. Though the temperature available in HAZ was lower but was sufficient to cause the dissolution of fine precipitates promoting the coarsening of grains in HAZ. Fine precipitates hindered the grain boundary movement and restricted the grain growth i.e. coarsening. On the other hand, dissolution greatly retarded the pinning effect, so easier grain boundary resulted in coarser grains in HAZ [48]. This grain coarsening increased the grain size larger than the other two weld zones and base metals.
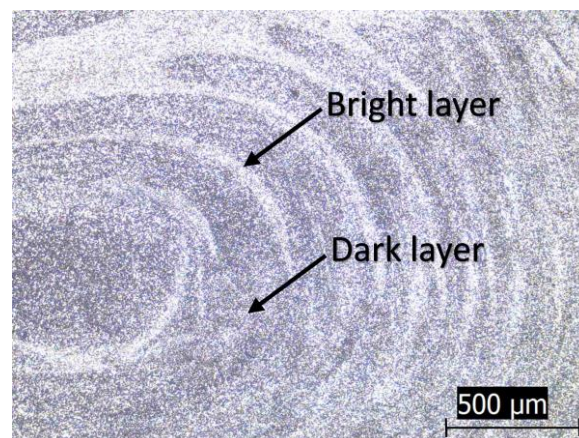

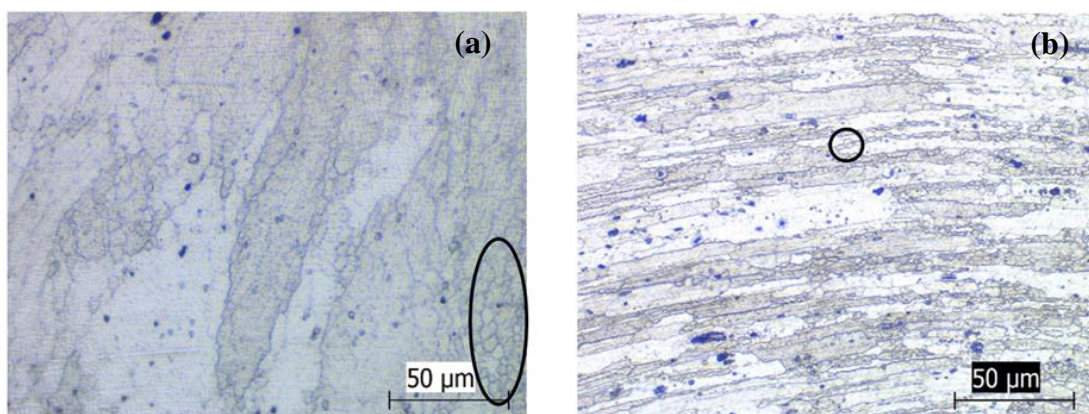*Figure 4. Onion rings formation at WS = 120 mm/min and RS = 1000 rpm.*

Figure 5. TMAZ of welded joints (a) AA2014 and, (b) AA7075.

3.1 Model Development and Statistical Analysis

Model development and entire statistical analysis reported in this work were carried out with the help of Design-Expert Software. Model selection is an important step in the analysis and was selected based on the

sum of squares, lack of fit, and model summary statistics. After this, the models were developed and analyzed with analysis of variance (ANOVA). If the R-Square statistics are satisfactory, then the next step of detailed analysis is carried out, otherwise, the backward elimination technique has been applied to enhance the adequacy of the model by eliminating the insignificant terms [49]. If the normality of residuals, constant error, outliers, and Box-Cox plot for power transforms were acceptable then the developed model can be recommended for further analysis.

Ultimate tensile Strength

ANOVA for the quadratic model of UTS after elimination of insignificant terms by backward elimination is presented in Table 4. The F-value of the model is determined by dividing the mean square value of the model by the mean square value of residual. Prob > F is the upper bound on P-value i.e. if a model represents a confidence level of 95% then it means that the terms with P value (Prob > F) larger than 0.05 were eliminated as insignificant terms during backward elimination. R-Squared value is interpreted as the proportion of the variability in the data explained by the ANOVA model. A difference greater than 0.20 between Predicted (Pred) R-squared and Adjusted (Adj) R-squared value indicates a problem with model/data [50]. Terms used here were only briefly described and the interested reader may refer to any standard text on the design of experiments for statistical details. It is evident from Table 4. that, A, B, and B^2 have a significant effect on UTS. R-Squared value of the model was obtained to be 0.8949. The Pred R-Squared value of 0.6647 was also in agreement with the Adj R-Squared value of 0.8498. The empirical equation to predict the UTS by this model is presented in Equation 1.

Table 4. Analysis of Variance for UTS.

Source	Sum of Squares	DF	Mean Square	F Value	P-value Prob > F	Contribution
Model	*11790.83*	*3*	*3930.28*	*19.86*	*0.0008*	
A-Welding Speed	*5182.04*	*1*	*5182.04*	*26.18*	*0.0014*	*39.33*
B-Rotary Speed	*2191.53*	*1*	*2191.53*	*11.07*	*0.0126*	*16.63*
B^2	*4417.25*	*1*	*4417.25*	*22.32*	*0.0021*	*33.52*
Residual	*1385.36*	*7*	*197.91*			*10.51*
Lack of Fit	*1272.69*	*5*	*254.54*	*4.52*	*0.1911*	*9.66*
Pure Error	*112.67*	*2*	*56.33*			*0.86*
Total	*13176.19*	*10*				

$$UTS = 172.82458 - 0.48981 \times WS + 0.45528 \times RS - 2.51531E\text{-}004 \times RS^2 \qquad (1)$$

Various plots for this model are presented in Figure 6. The normal probability plot shows the distribution of residuals. The points should fall along the straight line for the distribution to be normal. Points lying away from the straight line show the deviation from normal distribution however some scatter may occur for normal data also, so it is essential to look at the internally and externally studentized residuals. Residual versus predicted curve shows that internally studentized residuals lie within ±3σ whereas in the case of externally studentized residuals there is an outlier corresponding to run no. 5. To improve the normality of residuals, Box-Cox transformation has been used which is a family of power transformations that helps to easily find the optimal transformation for each variable. Power transformations raise the number to an exponent. Box-Cox transformation coefficient lambda (λ) indicates the power to which all data should be raised to normalize the data [51], [52]. In figure 6d, the blue line indicates the current value of λ whereas the green line recommends the best value of λ, so Box-Cox power transformation is required to make residuals normally distributed [52]. Figure 6d reveals that the best λ (green line) is 3, so power transform at λ=3 has been carried out.
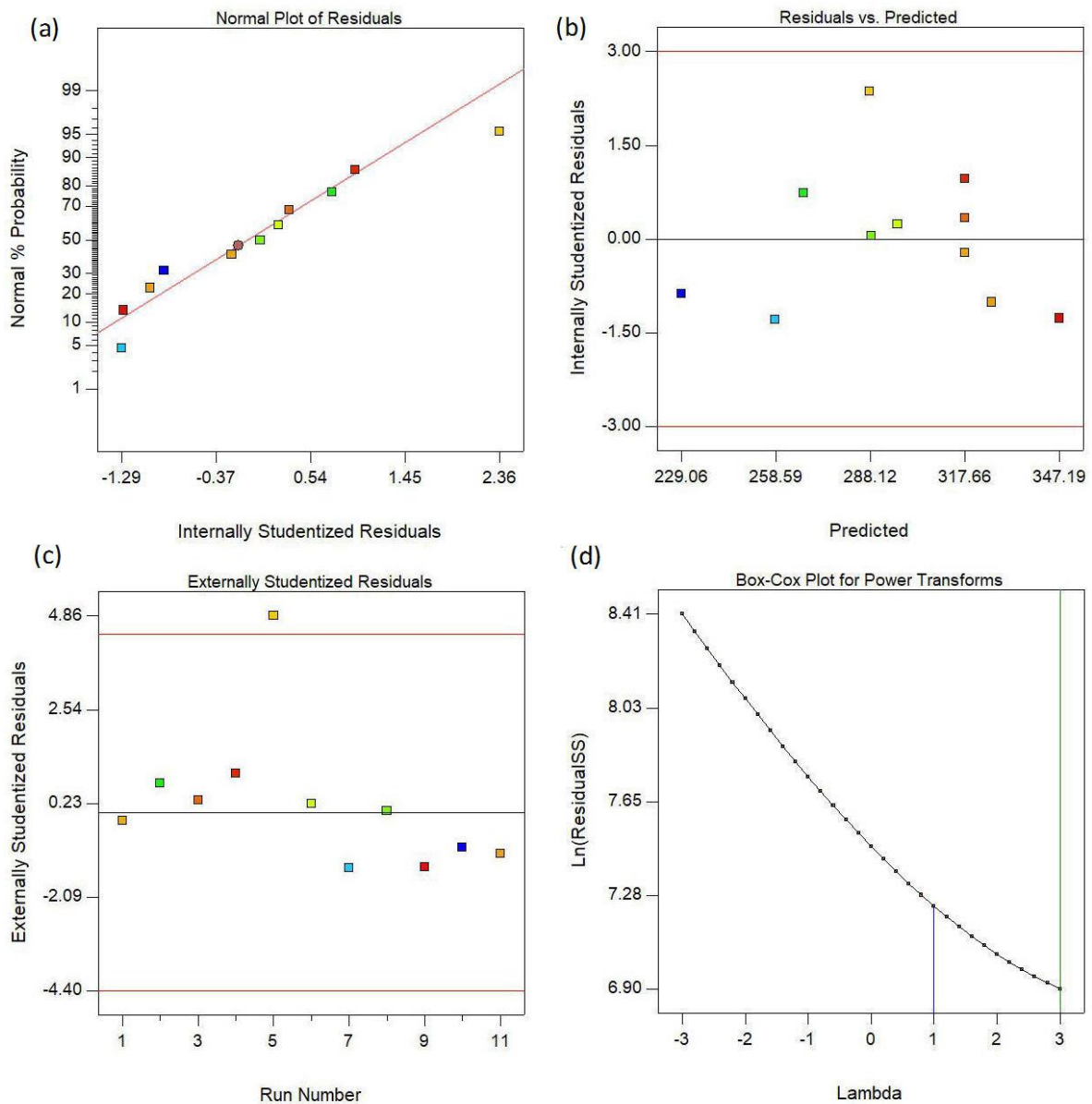
Figure 6. Various Plots for UTS (a) Normal plot of residuals, (b) Residuals versus predicted plot (c) Residuals versus run order plot and, (d) Box-Cox Plot.

The normal plot of residuals and externally studentized residuals after Box-Cox transformation are presented in Figure 6. The normal probability plot shows that the scatter of points around the straight line has been reduced in comparison to the non-transformation model and externally studentized residuals show no outlier after applying the Box-Cox transformation. It implies that the model can be used for further analysis.
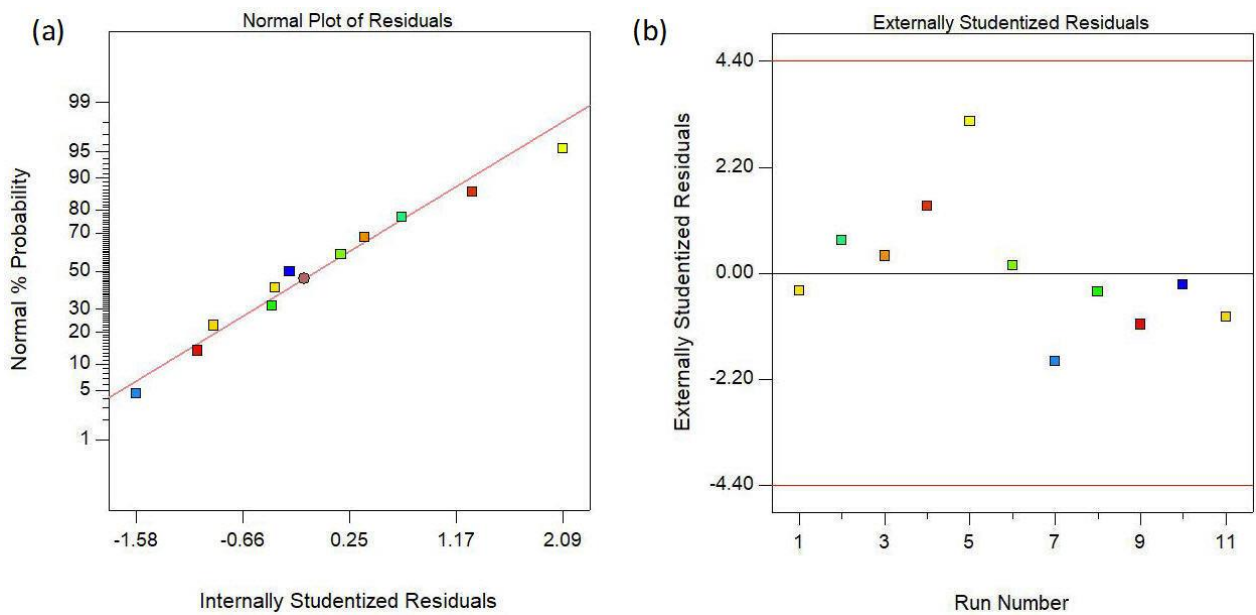
Figure 7. Various Plots for UTS after power transformation (a) Normal plot of residuals and, (b) Residuals versus run order plot.

ANOVA for the reduced quadratic model of UTS with Box-Cox transformation is presented in Table 5. Only A, B, and B^2 have a significant effect on UTS similar to the non-transformation model. The R-Squared statistics have been comparatively improved than the non-transformation model. R-Squared value of the model was improved to 0.9101. Also, the Pred R-Squared value of 0.7447 was in agreement with the Adj R-Squared value of 0.8716. An empirical equation to predict the UTS by utilizing the power transformation is presented in Equation 2.

Table 5. Analysis of Variance for UTS after power transformation at λ = 3.

Source	Sum of Squares	DF	Mean Square	F Value	P-value Prob > F	Contribution
Model	*6.722E+014*	*3*	*2.241E+014*	*23.63*	*0.0005*	
A-Welding Speed	*3.096E+014*	*1*	*3.096E+014*	*32.66*	*0.0007*	*41.92*
B-Rotary Speed	*9.406E+013*	*1*	*9.406E+013*	*9.92*	*0.0162*	*12.73*
B^2	*2.685E+014*	*1*	*2.685E+014*	*28.32*	*0.0011*	*36.35*
Residual	*6.637E+013*	*7*	*9.481E+012*			*8.99*
Lack of Fit	*5.538E+013*	*5*	*1.108E+013*	*2.02*	*0.3639*	*7.5*
Pure Error	*1.099E+013*	*2*	*5.493E+012*			*1.49*
Total	*7.386E+014*	*10*				

$$(UTS)^3 = -5.42191E+006 - 1.19725E+005 \times WS + 1.14133E+005 \times RS - 62.01581 \times RS^2 \quad (2)$$

Percentage Elongation and Defect-free status

ANOVA for reduced quadratic models of percentage elongation and defect-free status are presented in Tables 6 and 7 respectively. It is important to note that the response of defect-free status of the weld was kept +1 and −1 corresponding to Yes and No status of defects respectively. So the values obtained between +1 and −1 do not correspond to the size of the defect but only indicate the state of the defect. These models were developed for a confidence level of 95%. It was observed that only A, B, and B^2 had a significant effect on percentage elongation whereas only A and A^2 had a significant effect on defect-free status. The R-squared value of the % elongation model was calculated as 0.9633. Pred R-Squared value of 0.9151 was also in agreement with the Adj R-Squared value of 0.9476 for percentage elongation whereas R-Squared, Pred R-

Squared, and Adj R-Squared values are 1 for the defect-free status of welds. Regression equations to predict the percentage elongation and defect-free status by these models are presented in Equation 3 and 4 respectively. The residual plots were also found suitable to use the developed models for prediction and analysis as no variation/abnormality was observed. These plots are not presented here to remain focused on key issues.

Table 6. ANOVA for % elongation.

Source	Sum of Squares	DF	Mean Square	F Value	P-value Prob > F	Contribution
Model	20.76	3	6.92	61.25	< 0.0001	
A-Welding Speed	7.00	1	7.00	61.93	0.0001	32.48
B-Rotary Speed	5.47	1	5.47	48.43	0.0002	25.38
B^2	8.29	1	8.29	73.38	< 0.0001	38.47
Residual	0.79	7	0.11			3.67
Lack of Fit	0.53	5	0.11	0.82	0.6304	2.46
Pure Error	0.26	2	0.13			1.21
Total	21.55	10				

Table 7. ANOVA for Defect-free status.

Source	Sum of Squares	DF	Mean Square	F Value	p-value Prob > F	Contribution
Model	8.73	2	4.36	6.366E+007	< 0.0001	
A-Welding Speed	6.00	1	6.00	6.366E+007	< 0.0001	68.73
A^2	2.73	1	2.73	6.366E+007	< 0.0001	31.27
Residual	0.000	8	0.000			0
Lack of Fit	0.000	6	0.000			0
Pure Error	0.000	2	0.000			0
Cor Total	8.73	10				

$$\text{Percentage Elongation} = +1.01158 - 0.018 \times WS + 0.019408 \times RS - 1.08979E - 005 \times RS^2 \quad (3)$$

$$\text{Defect-free weld} = +5 - 0.083333 \times WS + 2.77778E - 004 \times WS^2 \quad (4)$$

3.2 Effect of welding parameters on response parameters

Effect of welding parameters on UTS

The strength of the developed weld joint depends on the selected process parameters. The process parameters mainly govern the heat generation in the weld region which in turn affects the material flow, grain structure, and precipitate morphology. The presence of any defect in the weld such as tunnels, pinholes, etc. not only affects the ultimate tensile strength adversely but also changes the fracture location that normally occurs in the minimum hardness region for a defect-free weld. Variation of UTS with WS and RS is shown in Figure 8. Weld strength of the dissimilar welds is generally limited by the strength of the weakest member. In this study, the UTS of all the welded joints was also found to be well below the UTS of the weakest alloy of combination i.e. AA2014. This may be attributed to the dissolution of the strengthening precipitates owing to dynamic recrystallization in WNZ during FSW that results in reduced strength.

The variation of UTS with WS and RS was shown in the form of a response surface graph and contour plot in Figure 8 a and b respectively. A continuous decrease in UTS was obtained with an increase in WS. With an increase in WS, the time of contact of the tool with the workpiece decreased, resulting in improper flow and mixing of materials on account of limited flowability due to reduced heat generation. UTS was found to increase with increasing RS from 600 rpm to 1000 rpm and then decreased with a further increase to 1400 rpm. An increase in RS results in more heat input that improves the flow and mixing owing to enhanced flowability. When heating is beyond optimal heat input then the tensile properties begin to deteriorate as can be observed

from Figure 8 a. Recrystallization forms strain-free fine grains. With an increase in heat input, the size of grains increases because of prolonged coarsening. The relation between strength and grain size is given by the Hall-Petch equation: $\sigma_y = \sigma_o + kd^{-1/2}$ where σ_y is yield strength, σ_o is resistance to dislocation motion, k is a constant and d is grain diameter. An inverse relationship between strength and grain diameter reveals that an increase in the value of the former will decrease the value of the latter and vice versa. Dynamic recrystallization results in fine grains and thus higher strength.
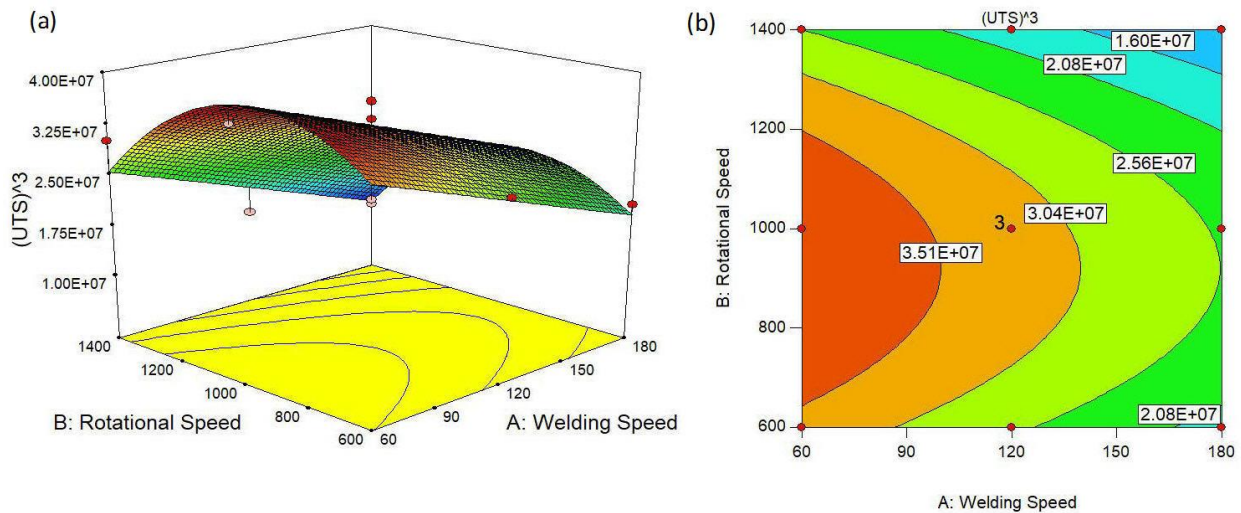
Figure 8. Effect of welding parameters on UTS (a) 3D Response surface graph and, (b) Contour plot.

Effect of welding parameters on % Elongation

Elongation at fracture is a measure of ductility which determines the ability of the material to flow plastically before fracture. It is usually represented in percentage. The variation of % elongation with WS and RS is shown in Figure 9.
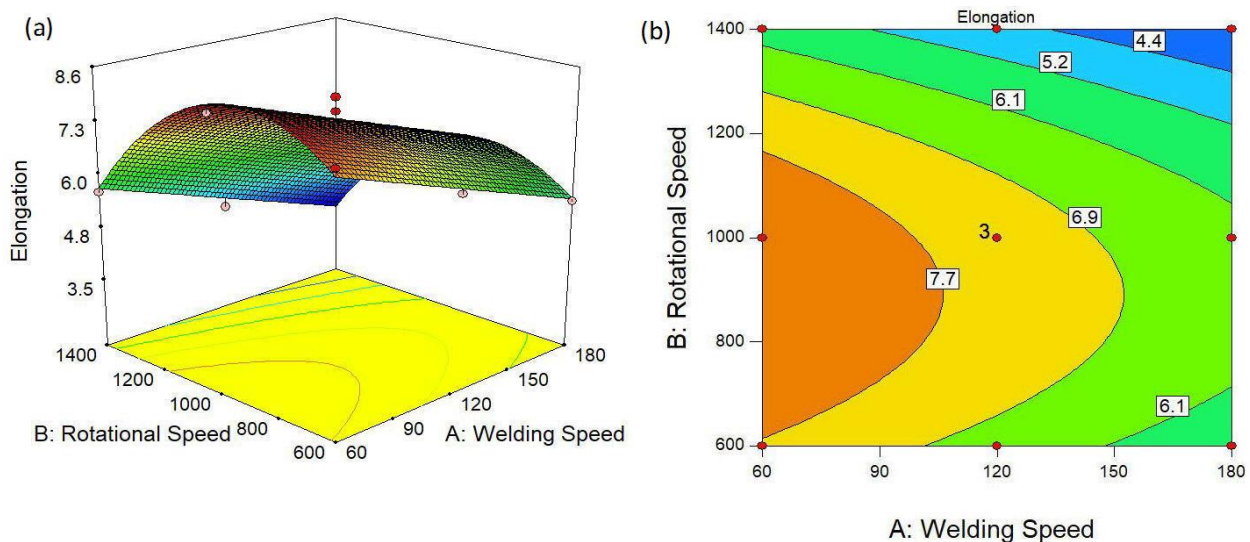

Figure 9. Effect of welding parameters on elongation (%) (a) 3D Response surface graph and, (b) Contour plot.

On comparing the trend of variation of percentage elongation with UTS, it was observed that both follow a similar trend for change in WS and RS. The elongation of base metals of AA2014 and AA7075 were 7.82% and 9.38%, respectively. Similar to UTS, maximum percentage elongation was achieved at WS of 60 mm/min

and RS of 1000 rpm but as opposed to UTS, % elongation was found higher than the % elongation of AA2014 base metal. Softening owing to the weld thermal cycle is responsible for reduced strength and higher ductility than the base metal. The contour plot in terms of possible combinations of RS and WS for percentage elongation is shown in Figure 9b. The curved lines in the contour plot show the lines of constant percentage elongation and can be used to determine the appropriate combination of WS and RS for a particular need.

Effect of welding parameter on defect-free weld

The selection of welding parameters is very crucial to obtain defect-free welded joints as they govern the mechanical properties of the welds. An optimum amount of heat generation is vital as the high heat input leads to grain growth whereas lower heat input results in inadequate flowability resulting in poor mixing and limited consolidation. High heat input results in defects like galling, excessive weld flash, etc., whereas low heat input leads to tunnel defect, kissing bond defect, joint lime remnant, etc. [1]. Obtaining a defect-free joint is the first and foremost objective for welded joints, as the defect either tunnel or pin size, adversely affects the mechanical strength and changes the fracture location. Apart from proper tool design, selection of appropriate dwell time, tool tilt, and plunge depth, RS and WS are also important. Figure 10 a and b depicts that defect-free welds were formed only at lowest WS and with further increase in WS they were more prone to generate defect as all the welds developed at higher WS have defects either macroscopic or microscopic. All the welds developed at the lowest WS at all combinations of the RS were defect-free whereas the welds developed at 180 mm/min and 600 rpm have a macroscopic defect. The formation of defect at the advancing side of this weld is attributed to the lowest heat generation resulting from poor material movement and consolidation behind the pin. Remaining all welds have very tiny microscopic voids in the nugget zone for remaining combinations of the RS.
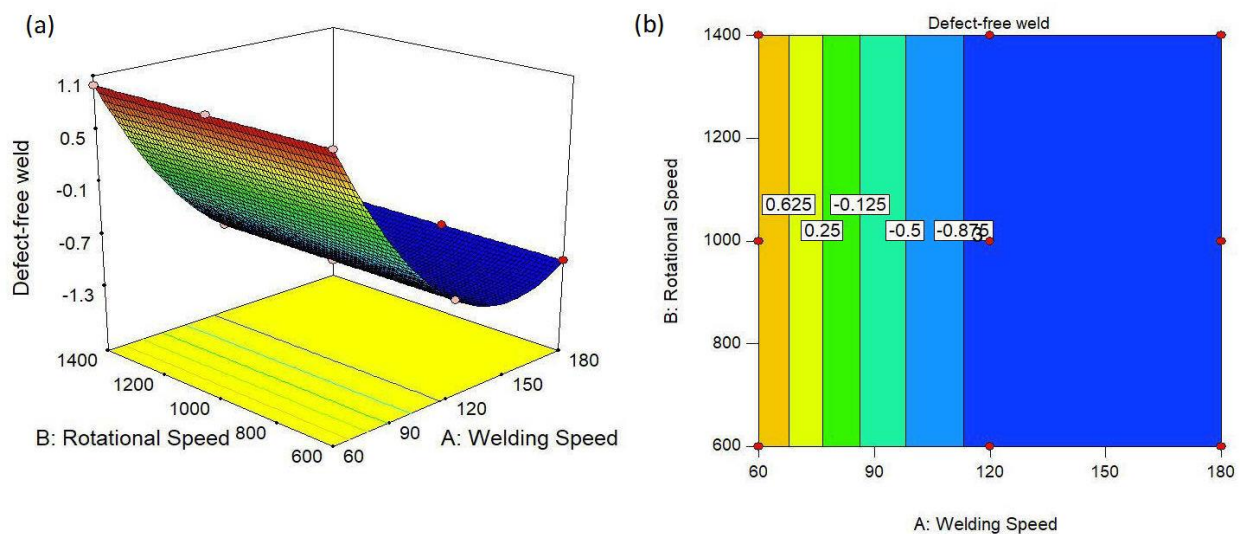

Figure 10. Effect of welding parameters on defect-free weld status (a) 3D Response surface graph and, (b) Contour plot.

3.3 Optimization

In this work, three responses were experimentally determined, and then by utilizing statistical techniques, a mathematical model for these responses have been developed. As multiple responses were involved in this problem, simultaneous optimization of all responses will ensure better quality weld joints. The desirability function approach is one of the popular techniques to deal with such optimization problems [49], [53]. In this approach, every response is transformed into its desirability function that ranges between zero and one. The individual desirability function was determined on the basis that whether the objective is to maximize, minimize, or to locate between the limits. In this study, the objective is to maximize the responses so the desirability function can be determined by the equation given below. The desirability function (d) is zero if

the response lies outside an acceptable region and is one when the response lies at the target. Design variables were then selected to maximize the overall desirability given by the following equations.

$$d_i = \begin{cases} 0 & y_i < L_i \\ \left[\dfrac{y_i - L_i}{T_i - L_i}\right]^t & , L_i < y_i < T_i \\ 1 & y_i > T_i \end{cases} \tag{5}$$

where y_i is response, L_i is lower bound and T_i is target and t is the weight.

$$D = (d_1 \times d_2 \times d_3 \times \dots\dots\dots \times d_m)^{\frac{1}{m}} \tag{6}$$

where m is the number of responses [50].

Limits, weights, and importance assigned to input and output response parameters for this work have been presented in Table 8.

Table 8. Parameter boundaries and importance assigned to each parameter for optimization.

Name	Goal	Lower Limit	Upper Limit	Lower Weight	Upper Weight	Importance
WS	is in range	60	180	1	1	3
RS	is in range	600	1400	1	1	3
UTS	maximize	220.33	333	1	1	3
Elongation	maximize	3.91	8.24	1	1	3
Defect-free weld	maximize	−1	1	1	1	3

An optimal combination resulting in maximum desirability of one has been presented in Table 9. RS has been selected as 1000 rpm for confirmation instead of the desirability analysis value of 1008.62 rpm to make its value more rational for further experimental work and scientific discussion. The proximity of the predicted values and experimental values confirms the validity of the results.

Table 9. Comparison of predicted and experimental values at optimal combination of parameters.

	WS (mm/min)	RS (rpm)	UTS (MPa)	Elongation (%)	Defect-free status
Predicted	60	1008.62	340	8.40	1
Experimental	60	1000	333	8.24	1

4   Microstructural and Mechanical Properties of Optimum weld

4.1 Microstructure

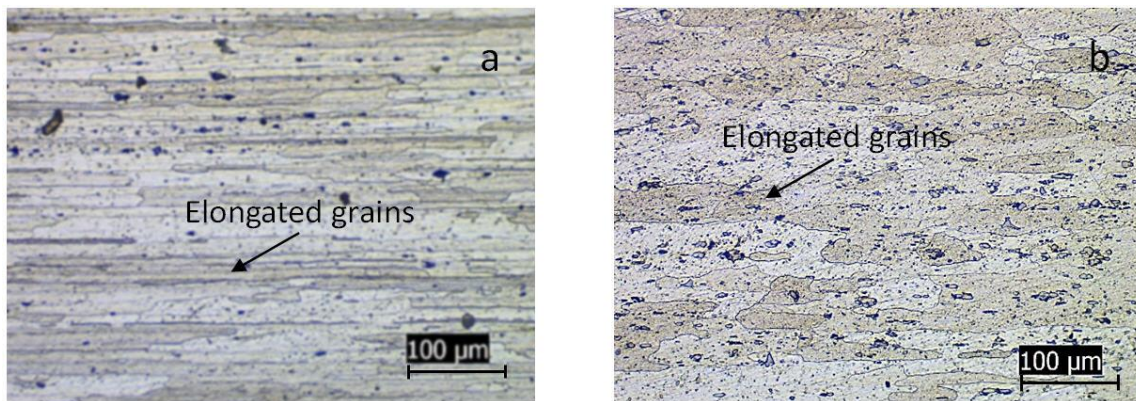The microstructure of base materials AA2014 and AA7075 are presented in Figure 11.

Figure 11. Microstructure of base metals (a) AA7075 and, (b) AA2014.

Grains of AA7075 were elongated in rolling direction with the grain size of ~100 µm in length and width of ~12 µm whereas grains of AA2014 were smaller but broader than the AA7075 grains having a length of ~62 µm and width of ~19 µm.

The microstructure of the weld nugget center corresponding to optimum weld (OW), lowest heat input weld (LIW), and highest heat input weld (HIW) are shown in Figure 12. The grain size of OW, LIW, and HIW is 2.819 ± 1.077, 2.187 ± 0.719, and 2.692 ± 1.207 µm respectively. FSW has not only reduced the size of grains drastically but also make them axisymmetric irrespective of weld parameters. The grain size was found lowest for LIW and highest for OW.
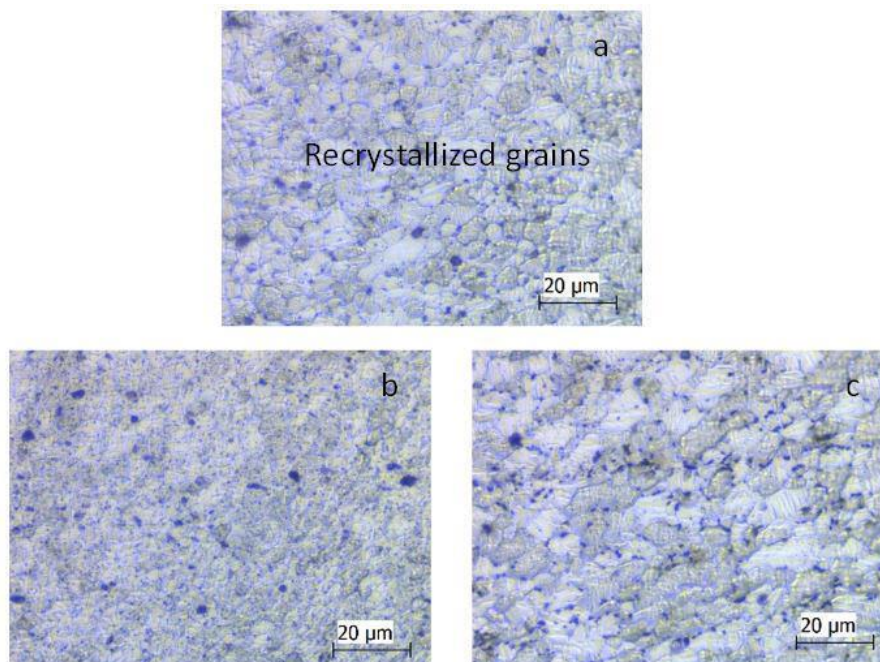

Figure 12. Microstructure at the center of the WNZ for (a) OW [RS 1000 WS 60] (b) LIW [RS 600 WS 180] and, (c) HIW [RS 1400 WS 60].

4.2 Tensile Strength

Tensile Strength, percentage elongation, and joint efficiency of the weld joints developed at OW, LIW, and HIW combination of process parameters are shown in Figure 13. The tensile strength of the welded joints depends on the presence of macroscopic defects, degree of plastic deformation and mixing, grain size, degree of dissolution, and over the aging of precipitates [54]. These factors in turn can be effectively controlled by

appropriate weld parameters as they determine (i) heat generation (ii) peak temperature and (iii) solute concentration of strengthening precipitates in the aluminum matrix.

The first two factors improve flowability on account of reduced flow stresses so better bonding of material occurs. The third factor promotes the re-precipitation on account of effective post-weld aging. Therefore, better bonding, high density of fine re-precipitated strengthening particles resulted in the highest tensile strength at OW combination. On other hand, the reduced tensile strength of LIW joints was primarily due to the reduced plasticization and improper flow of material resulting in voids on the advancing side. At the highest RS and lowest WS, maximum peak temperature was available for a longer duration so the reduction in tensile strength of HIW joints may be attributed to the coarsening of reprecipitated strengthening particles. Also, the elongation of the welded joint at the various combination of parameters presented a similar trend to the strength of the welded joints as evident from Figure 13. The highest tensile strength of 333 MPa, 8.24% elongation of, and 71% joint efficiency was obtained for OW. Joint efficiency is measured by dividing the strength of welds by the strength of the weakest base metal to be welded [55]. Low percentage elongation was observed for the welded joint that fractured from the WNZ than those fractured from TMAZ/HAZ. The optimum combination was at RS of 1000 rpm and WS of 60 mm/min that produced the best strength, elongation, and percentage elongation.
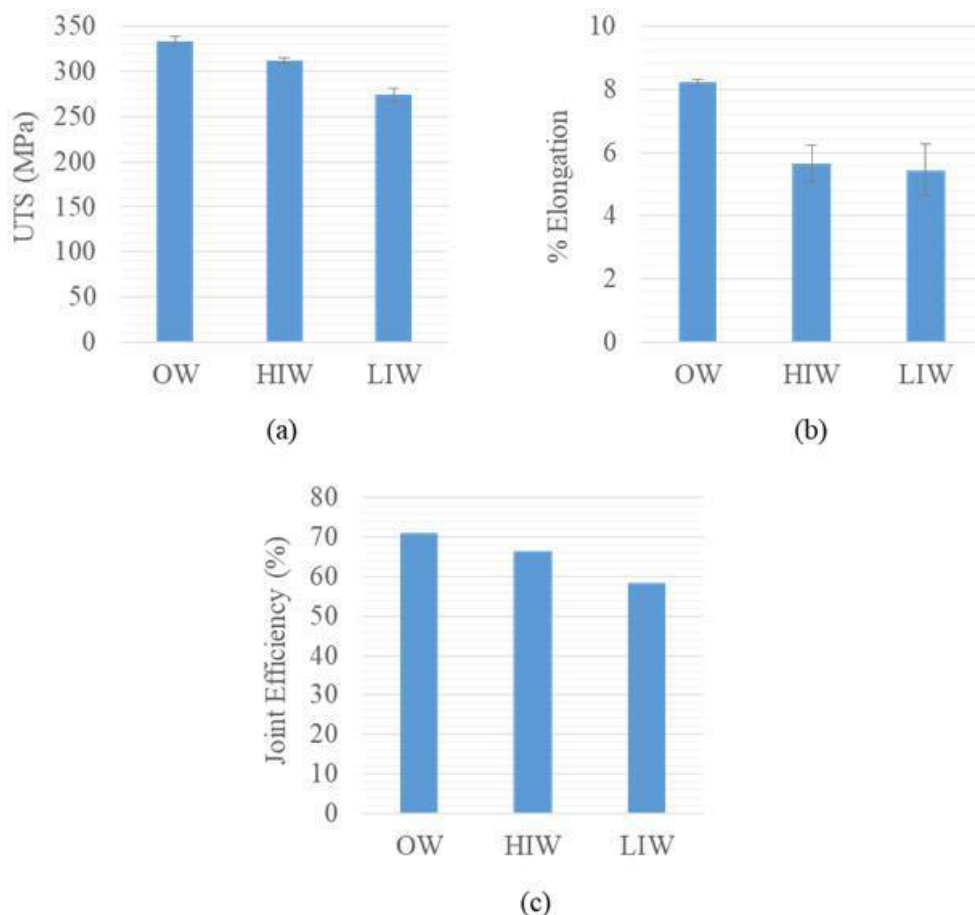

Figure 13. (a) Tensile strength, (b) Percentage elongation, and (c) Joint efficiency of the welded joints.
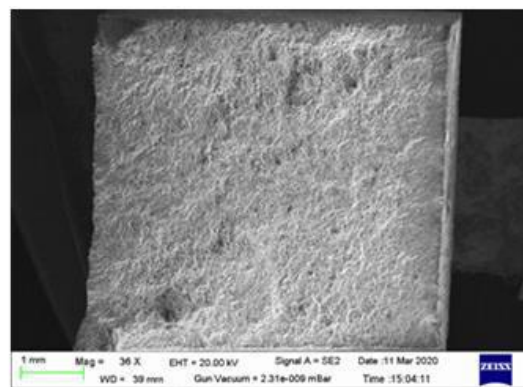
4.3 Fracture

The fracture surface of tensile specimens was observed by SEM using samples from failure location i.e. advancing side (AA2014) of the welded joints. SEM images of low and high magnification of the fractured surface of welded joints developed at OW, LIW, and HIW combination of process parameters are presented in Figure 14 and 15. At low magnification image (Figure 14) of OW and HIW the fracture was flat while at LIW a trench was observed throughout the surface which indicate poor consolidation of material throughout the joint resulting in macroscopic defect. In high magnification image (Figure 15), Though all the fracture
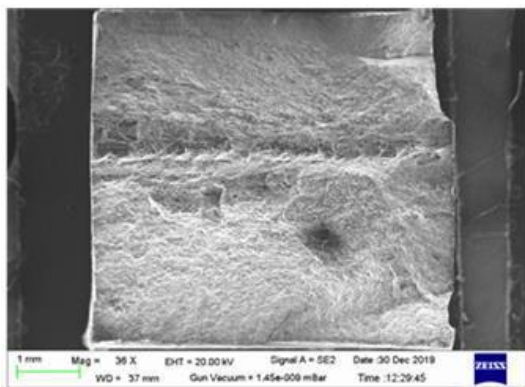
surfaces were covered with dimples, the morphology of the fracture was significantly different as evident from the SEM images of welded joints.

The fracture surface of LIW joints was uneven and exhibited the least population of shallow dimples. Secondary precipitates were also observed in abundance inside the dimples. There were few large dimples also containing fractured secondary precipitates. The presence of secondary precipitates in abundant over fracture surface confirms the dominance of coarsening over re-precipitation owing to the lowest heat input. A crack was present in the center of the fracture surface and seems to form due to the tearing of loosely consolidated materials. Further, agglomeration indicates poor consolidation of deformed material in WNZ. It can be argued that the poor consolidation resulted in the formation of a macroscopic defect in the LIW joint which initiated the fracture of welded joints, which is shown in Figure 15 (b). Coarsening coupled with the absence of void formation and coalescence can be held responsible for low strength and elongation of LIW joints that underwent mix mode failure.
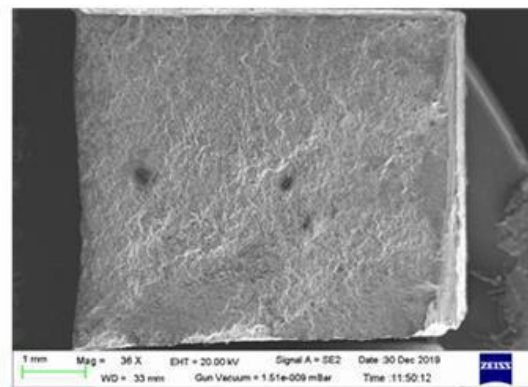
The fracture surface of OW joints was even and covered with dimples of the approximately same size. Featureless flat regions were scattered all over the fractured surface. As compared to LIW joints, secondary precipitates could not be observed on the fracture surface of the OW joint. This indicates the dominance of re-precipitation over coarsening owing to better dissolution on account of high heat input. The. appearance of the fracture surface of HIW joints was similar to OW joint. The dimples were large and contain secondary precipitates while flat featureless regions were few and small. The OW and HIW joints exhibited a ductile mode of fracture.
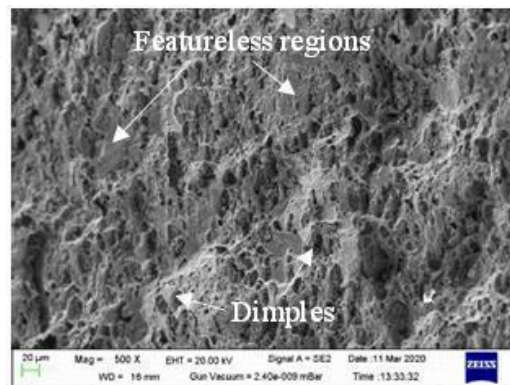

Figure 14. Low magnification image of fracture surface of (a) Optimum weld (OW) (b) Lowest heat input weld (LIW) and, (c) Highest heat input weld (HIW).

(a) Optimum Weld (OW)

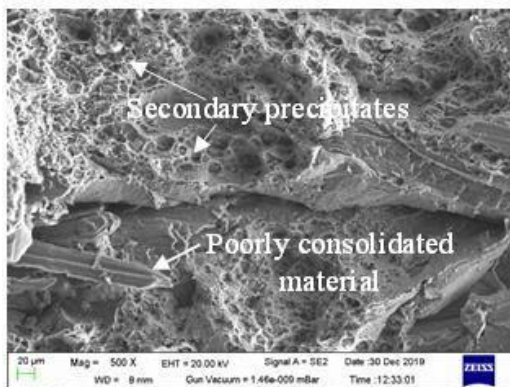(b) Lowest heat input weld (LIW)   (c) Highest heat input weld (HIW)

Figure 15. The fracture surface of (a) Optimum weld (OW) (b) Lowest heat input weld (LIW) and, (c) Highest heat input weld (HIW).

5 Conclusion

In this work, response data obtained from experiments conducted as per CCD of RSM has been used to develop regression models and multi-response optimization of process parameters in FSW of AA2014 and AA7075 dissimilar alloys. Models were developed for UTS, % elongation, and defect-free status of welds. Box-cox transformation has been used to deal with external studentized residuals lying beyond the prescribed limits and the regression model for UTS was developed by using power transform at λ=3. Optimal parameters were determined as 60 mm/min welding speed and 1000 rpm rotary speed by the desirability function approach to produce defect-free welded joints. Grain size in WNZ of OW joints was found significantly smaller than both the base metals. Also, the fracture surface of OW joints was even and covered with dimples of approximately the same size indicating the ductile mode of fracture.

References

[1] N. Z. Khan, A. N. Siddiquee, and Z. A. Khan, *Friction stir welding: Dissimilar aluminum alloys*. CRC Press, 2017.

[2] N. Z. Khan *et al.*, "Microstructural features of friction stir welded dissimilar Aluminium alloys AA2219-AA7475," *Mater. Res. Express*, vol. 5, no. 5, p. 056531, May 2018.

[3] Z. Zhang, B. L. Xiao, and Z. Y. Ma, "Influence of water cooling on microstructure and mechanical properties of friction stir welded 2014Al-T6 joints," *Mater. Sci. Eng. A*, vol. 614, pp. 6–15, Sep. 2014.

[4] K. Mroczka, A. Wójcicka, and A. Pietras, "Characteristics of dissimilar FSW welds of aluminum alloys 2017A and 7075 on the basis of multiple layer research," *J. Mater. Eng. Perform.*, vol. 22, no. 9, pp.

_____

2698–2705, 2013.

[5]   G. İpekoğlu, S. Erim, B. Gören Kıral, and G. Çam, "Investigation into the effect of temper condition on friction stir weldability of AA6061 Al-alloy plates," *Kovove Mater.*, vol. 51, no. 3, pp. 155-163, 2013.

[6]   G. İpekoğlu, S. Erim, and G. Çam, "Effects of temper condition and post weld heat treatment on the microstructure and mechanical properties of friction stir butt welded AA7075 Al-alloy plates," *Int. J. Adv. Manuf. Technol.*, vol. 70, no. 1, pp. 201-213, 2014.

[7]   M. Grujicic, G. Arakere, H. V. Yalavarthy, T. He, C. F. Yen, and B. A. Cheeseman, "Modeling of AA5083 material-microstructure evolution during butt friction-stir welding," *J. Mater. Eng. Perform.*, vol. 19, no. 5, pp. 672–684, 2010.

[8]   G. Çam and S. Mistikoglu, "Recent developments in friction stir welding of al-Alloys," *J. Mater. Eng. Perform.*, vol. 23, no. 6, pp. 1936–1953, 2014.

[9]   A. Heidarzadeh, S. Mironov, R. Kaibyshev, G. Çam, A. Simar, A. Gerlich, F. Khodabakhshi, A. Mostafaei, D. P. Field, J. D. Robson, A. Deschamps and P.J. Withers, "Friction stir welding/processing of metals and alloys: A comprehensive review on microstructural evolution.," *Prog. Mater. Sci.*, vol. 117, 2021.

[10]   N. Kashaev, V. Ventzke, and G. Çam, "Prospects of laser beam welding and friction stir welding processes for aluminum airframe structural applications," *J. Manuf. Processes*, vol. 36, pp. 571-600, 2018.

[11]   G. Çam and G. İpekoğlu, Recent developments in joining of aluminium alloys, Int. J. Adv. Manuf. Technol., vol. 91, no. 5-8, pp. 1851-1866, 2017.

[12]   G. Çam, "Friction Stir Welded Structural Materials: Beyond Al-Alloys," *Int. Mater. Rev.*, vol. 56, no. 1, pp. 1-48, 2011.

[13]   A. Von Strombeck, G. Çam, J. F. Dos Santos, V. Ventzke, and M. Koçak, "A Comparison Between Microstructure, Properties, and Toughness Behavior of Power Beam and Friction Stir Welds in Al-Alloys," Proc. of the TMS 2001 Annual Meeting Aluminum, Automotive and Joining (New Orleans, Louisiana, USA, February 12-14, 2001), eds: S.K. Das, J.G. Kaufman, and T.J. Lienert, pub.: TMS, Warrendale, PA, USA, pp. 249-264, 2001.

[14]   G. İpekoğlu, S. Erim, and G. Çam, "Investigation into the influence of post-weld heat treatment on the friction stir welded AA6061 Al-alloy plates with different temper conditions," *Metall. Mater. Trans. A*, vol. 45A, no. 2, pp. 864-877, (2014).

[15]   N. Mendes, P. Neto, A. Loureiro, and A. P. Moreira, "Machines and control systems for friction stir welding: A review," *Mater. Des.*, vol. 90, pp. 256–265, 2016.

[16]   M. Pakdil, G. Çam, M. Koçak, and S. Erim, "Microstructural and mechanical characterization of laser beam welded AA6056 Al-alloy," *Mater. Sci. Eng. A*, vol. 528, no. 24, pp. 7350-7356, 2011.

[17]   G. Çam and M. Koçak, "Microstructural and mechanical characterization of electron beam welded Al-alloy 7020," *J. Mater. Sci.*, vol. 42, no. 17, pp. 7154-7161, 2007.

[18]   G. Çam, V. Ventzke, J.F. dos Santos, M. Koçak, G. Jennequin, and P. Gonthier-Maurin, "Characterisation of electron beam welded aluminium alloys," *Sci. Technol. Weld. Join.*, vol. 4, no. 5, pp. 317-323, 1999.

[19]   G. Çam, V. Ventzke, J.F. dos Santos, M. Koçak, G. Jennequin, P. Gonthier-Maurin, M. Penasa, and C. Rivezla, "Characterization of laser and electron beam welded Al-alloys," *Prakt. Metallogr.*, vol. 36, no. 2, pp. 59-89, 1999.

[20]   H. Robe, Y. Zedan, J. Chen, H. Monajati, E. Feulvarch, and P. Bocher, "Microstructural and mechanical characterization of a dissimilar friction stir welded butt joint made of AA2024-T3 and AA2198-T3," *Mater. Charact.*, vol. 110, pp. 242–251, 2015.

[21]   J. F. Guo, H. C. Chen, C. N. Sun, G. Bi, Z. Sun, and J. Wei, "Friction stir welding of dissimilar materials between AA6061 and AA7075 Al alloys effects of process parameters," *Mater. Des.*, vol. 56, pp. 185–192, 2014.

[22]   G. İpekoğlu and G. Çam, "Effects of initial temper condition and postweld heat treatment on the properties of dissimilar friction-stir-welded joints between AA7075 and AA6061 aluminum alloys," *Metall. Mater. Trans. A*, vol. 45, no. 7, pp. 3074-3087, 2014.

[23]   G. Çam, G. İpekoğlu, and H.T. Serindağ, "Effects of use of higher strength interlayer and external cooling on properties of friction stir welded AA6061-T6 joints, *Sci. Technol. Weld. Join.*," vol. 19, no.

_____

8, pp. 715-720, 2014.

[24]   S. A. Khodir and T. Shibayanagi, "Friction stir welding of dissimilar AA2024 and AA7075 aluminum alloys," *Mater. Sci. Eng. B Solid-State Mater. Adv. Technol.*, vol. 148, no. 1–3, pp. 82–87, 2008.

[25]   A. A. M. da Silva, E. Arruti, G. Janeiro, E. Aldanondo, P. Alvarez, and A. Echeverria, "Material flow and mechanical behaviour of dissimilar AA2024-T3 and AA7075-T6 aluminium alloys friction stir welds," *Mater. Des.*, vol. 32, no. 4, pp. 2021–2027, 2011.

[26]   M. M. Hasan, M. Ishak, and M. R. M. Rejab, "Effect of pin tool flute radius on the material flow and tensile properties of dissimilar friction stir welded aluminum alloys," *Int. J. Adv. Manuf. Technol.*, vol. 98, no. 9–12, pp. 2747–2758, Oct. 2018.

[27]   B. K. B. Nadikudi, M. J. Davidson, N. R. Akasapu, and M. Govindaraju, "Formability analysis of dissimilar tailor welded blanks welded with different tool pin profiles," *Trans. Nonferrous Met. Soc. China (English Ed.*, vol. 25, no. 6, pp. 1787–1793, Jun. 2015.

[28]   P. Alvarez, G. Janeiro, A. A. M. Da Silva, E. Aldanondo, and A. Echeverría, "Material flow and mixing patterns during dissimilar FSW," *Science and Technology of Welding and Joining*, vol. 15, no. 8. pp. 648–653, 2010.

[29]   C. Jonckheere, B. De Meester, A. Denquin, and A. Simar, "Torque, temperature and hardening precipitation evolution in dissimilar friction stir welds between 6061-T6 and 2014-T6 aluminum alloys," *J. Mater. Process. Technol.*, vol. 213, no. 6, pp. 826–837, 2013.

[30]   C. Sharma and V. Upadhyay, "Friction Stir Welding of Dissimilar Aluminum Alloys AA5086 and AA7039," *J. Phys. Conf. Ser.*, vol. 1240, no. 1, 2019.

[31]   A. Barbini, J. Carstensen, and J. F. Dos Santos, "Influence of alloys position, rolling and welding directions on properties of AA2024/AA7050 dissimilar butt weld obtained by friction stirwelding," *Metals (Basel).*, vol. 8, no. 4, 2018.

[32]   Saravanan, N. Banerjee, R. Amuthakkannan, and S. Rajakumar, "Microstructural Evolution and Mechanical Properties of Friction Stir Welded Dissimilar AA2014-T6 and AA7075-T6 Aluminum Alloy Joints," *Metallogr. Microstruct. Anal.*, vol. 4, no. 3, pp. 178–187, 2015.

[33]   S. Singh and G. Dhuria, "Investigation of post weld cryogenic treatment on weld strength in friction stir welded dissimilar aluminium alloys AA2014-T651 and AA7075-T651," in *Mater. Today: Proc.*, 2017, vol. 4, no. 8, pp. 8866–8873.

[34]   V. Pandian and S. Kannan, "Numerical prediction and experimental investigation of aerospace-grade dissimilar aluminium alloy by friction stir welding," *J. Manuf. Process.*, vol. 54, pp. 99–108, Jun. 2020.

[35]   A. Heidarzadeh, H. Khodaverdizadeh, A. Mahmoudi and E. Nazari, "Tensile behavior of friction stir welded AA 6061-T4 aluminum alloy joints," *Mater. Des.*, vol. 37, pp.   166–173, 2012.

[36]   A. Heidarzadeh and T. Saeid, "Correlation between process parameters, grain size and hardness of friction-stir-welded Cu–Zn alloys," *Rare Metals*, 2016.

[37]   A. Heidarzadeh, P. Motalleb-nejad, R.V. Barenji, V. Khalili and Gü. Güleryüz, "The bead on plate friction stir welding of a single phase brass: Elucidating the origins of the maximum hardness," *Mater. Chem. Phys.,* 2018. doi: https://doi.org/10.1016/j.matchemphys.2018.10.033.

[38]   A. heidarzadeh, "Tensile behavior, microstructure, and substructure of the friction stir welded 70/30 brass joints: RSM, EBSD, and TEM," *Arch. Civ. Mech. Eng.*, vol. 19, pp. 137- 146, 2019.

[39]   A. Heidarzadeh, R. V. Barenji, V. Khalili and Gü. Güleryüz, "Optimizing the friction stir welding of the α/β brass plates to obtain the highest strength and elongation," *Vacuum,* 2018, doi: https://doi.org/10.1016/j.vacuum.2018.10.036.

[40]   A. Heidarzadeh, M. Paidar, G. Güleryüz and R. Vatankhah Barenji, "Application of nanoindentation to evaluate the hardness and yield strength of brass joints produced by FSW: microstructural and strengthening mechanisms," *Arch. Civ. Mech. Eng.*, vol. 20, no. 41, 2020.

[41]   R. Crawford, G. E. Cook, A. M. Strauss, D. A. Hartman, and M. A. Stremler, "Experimental defect analysis and force prediction simulation of high weld pitch friction stir welding," *Sci. Technol. Weld. Join.*, vol. 11, no. 6, pp. 657–665, 2006.

[42]   T. U. Seidel and A. P. Reynolds, "Visualization of the material flow in AA2195 friction-stir welds using a marker insert technique," *Metall. Mater. Trans. A Phys. Metall. Mater. Sci.*, vol. 32, no. 11, pp. 2879–2884, 2001.

[43]   H. J. McQueen, M. Cabibbo, and E. Evangelista, "Piercing/extrusion and FSW nugget microstructure formation in Al alloys," *Mater. Sci. Technol.*, vol. 23, no. 7, pp. 803–809, 2007.

[44]   M. M. Moradi, H. Jamshidi Aval, R. Jamaati, S. Amirkhanlou, and S. Ji, "Microstructure and texture evolution of friction stir welded dissimilar aluminum alloys: AA2024 and AA6061," *J. Manuf. Process.*, vol. 32, pp. 1–10, 2018.

[45]   J. –Q. Su, T. W. Nelson and C. J. Sterling, "Microstructure evolution during FSW/FSP of high strength aluminum alloys," *Mater. Sci. Eng.: A*," Vol. 405, pp. 277-286, 2005.

[46]   C. G. Rhodes, M. W. Mahoney, W. H. Bingel and M. Calabrese, "Fine-grain evolution in frictionstir processed 7050 aluminum. *Scr. Mater.*," Vol. 48, pp. 1451-55, 2003.

[47]   J. -Q. Su, T. W. Nelson and C. J. Sterling, "Grain refinement of aluminum alloys by friction stir processing. *Philos. Mag.*," Vol. 86, pp. 1-24, 2006.

[48]   C. Sharma, D. K. Dwivedi, and P. Kumar, "Influence of pre-weld temper conditions of base metal on microstructure and mechanical properties of friction stir weld joints of Al-Zn-Mg alloy AA7039," *Mater. Sci. Eng. A*, vol. 620, pp. 107–119, Jan. 2015.

[49]   S. Verma, M. Gupta, and J. P. Misra, "Optimization of process parameters in friction stir welding of armor-marine grade aluminium alloy using desirability approach," *Mater. Res. Express*, vol. 6, no. 2, 2019.

[50]   D. Montgomery, "Design and Analysis of Experiments," *Wiley, India*, 2007. [Online]. Available: https://www.wileyindia.com/design-and-analysis-of-experiments-8th-ed-isv.html. [Accessed: 19-Nov-2020].

[51]   J. W. Osborne, "Improving your data transformations: Applying the Box-Cox transformation," *Pract. Assessment, Res. Eval.*, vol. 15, no. 12, 2010.

[52]   B. Bhardwaj, R. Kumar, and P. K. Singh, "An improved surface roughness prediction model using Box-Cox transformation with RSM in end milling of EN 353," *J. Mech. Sci. Technol.*, vol. 28, no. 12, pp. 5149–5157, 2014.

[53]   K. Ravi Kumar and Nishasoms, "Desirability-Based Multi-objective Optimization and Analysis of WEDM Characteristics of Aluminium (6082)/Tungsten Carbide Composites," *Arab. J. Sci. Eng.*, vol. 44, no. 2, pp. 893–909, 2019.

[54]   R. Palanivel, P. Koshy Mathews, N. Murugan, and I. Dinaharan, "Effect of tool rotational speed and pin profile on microstructure and tensile strength of dissimilar friction stir welded AA5083-H111 and AA6351-T6 aluminum alloys," *Mater. Des.*, vol. 40, pp. 7–16, 2012.

[55]   L. Giraud, H. Robe, C. Claudin, C. Desrayaud, P. Bocher, and E. Feulvarch, "Investigation into the dissimilar friction stir welding of AA7020-T651 and AA6060-T6," *J. Mater. Process. Technol.*, vol. 235, pp. 220–230, 2016.